https://doi.org/10.22226/2410-3535-2021-3-309-314 PACS: 47.35.+i, 87.64.Ee, 81.70.Bt

The mechanism of formation of surface micro- and nanostructures in the AlCoCrFeNi high-entropy alloy during electron-beam treatment

S. A. Nevskii[1], S. V. Konovalov[†,1,2], K. A. Osintsev[1,2], Yu. F. Ivanov[1,3],

A. Y. Granovskii[1], V. E. Gromov[1]

[†]ksv@ssau.ru

[1]Siberian State Industrial University, Novokuznetsk, 654007, Russia
[2]Samara National Research University, Samara, 443086, Russia
[3]Institute of High Current Electronics SB RAS, Tomsk, 634055, Russia

The paper is devoted to a study of the formation of submicron and nanosized cellular crystallization structures on the surface of a high-entropy AlCoCrFeNi alloy irradiated by high current electron beams with the energy density varying from 10 to 30 J/cm^2 and a pulse time of 200 μs. The study revealed that the combination of thermal, evaporation-capillary and thermoelectric instabilities induces the formation of submicro- and nanodimensional cellular structures similarly to high-entropy alloys. The proposed dispersion equation was analyzed to detect the conditions for the generation of this instability. The importance of the evaporation process was investigated by finding a solution to the heat problem with phase transformations. The temperature distribution over time calculated at different distances from the surface of the alloy samples demonstrated that the surface temperature is lower than the evaporation temperature for the energy density $E_s < 30$ J/cm^2, therefore, the term of evaporation in the dispersion equation was ignored for these values of the energy density. The analysis of the dispersion equation showed that for $E_s = 30$ J/cm^2, the wavelength λ_m with the maximal growth rate of perturbations on the melt surface gains a value in the submicro-and nano-range, provided that the thermoelectric coefficient equals to ~4 –10 V/K, and the pressure of evaporation is ~10^5 Pa. If we exclude thermoelectric effects, these values λ_m are observed for the pressure of evaporation ~10^{11} Pa. The wavelength λ_m was revealed to decrease according to a power law as the beam energy density increases.

Keywords: high-entropy alloys, AlCoCrFeNi, electron beam treatment, thermocapillary instability, thermoelectric effect.

УДК: 532.5; 539.8

Механизм формирования поверхностных микро- и наноструктур в высокоэнтропийном AlCoCrFeNi сплаве при электронно-пучковой обработке

Невский С. А.[1], Коновалов С. В.[†,1,2], Осинцев К. А.[1,2], Иванов Ю. Ф.[1,3],

Грановский А. Ю.[1], Громов В. Е.[1]

[1]Сибирский государственный индустриальный университет, Новокузнецк, 654007, Россия
[2]Самарский национальный исследовательский университет им. С. П. Королева, Самара, 443086, Россия
[3]Институт сильноточной электроники СО РАН, Томск, 634055, Россия

Изучено формирование структуры ячеистой кристаллизации субмикро- и наноразмерного диапазона на поверхности высокоэнтропийного сплава AlCoCrFeNi при воздействии низкоэнергетических сильноточных электронных пучков с плотностями энергии от 10 до 30 Дж/см^2 и длительностью импульса 200 мкс. Установлено, что также как и для двух- и трёхкомпонентных сплавов причиной образования субмикро- и наноразмерных ячеистых структур является комбинированная неустойчивость, которая включает в себя термо-, испарительно-капиллярную и термоэлектрическую неустойчивости. Для выявления условий зарождения этой неустойчивости анализировалось предложенное в предыдущих работах авторов дисперсионное уравнение. Роль процесса испарения выявлялась путем

решения тепловой задачи с учетом фазовых переходов. Расчеты распределения температур по времени на различных расстояниях от поверхности образцов данного сплава показали, что при значении плотности энергии $E_s < 30$ Дж/см^2 температура поверхности не достигает температуры испарения, поэтому при данных значениях плотности энергии испарительный член дисперсионного уравнения не учитывался. Результаты анализа дисперсионного уравнения показали, что при $E_s = 30$ Дж/см^2 длина волны λ_m, на которую приходится максимум скорости роста возмущений поверхности расплава, принимает значение, находящееся в субмикро и нанодипазоне, при условии, что значение термоэлектрического коэффициента будет составлять ~4–10 В/К, а значение испарительного давления ~10^5 Па. Если не учитывать термоэлектрические эффекты, то такие значения λ_m наблюдается только при испарительном давлении ~10^{11} Па. Показано, что λ_m уменьшается с ростом плотности энергии пучка электронов по степенному закону.

Ключевые слова: высокоэнтропийные сплавы, AlCoCrFeNi, электронно-пучковая обработка, термокапиллярная неустойчивость, термоэлектрический эффект.

1. Introduction

In recent years, the effect of concentrated energy flows, e. g. low energy high current electron beams on high-entropy alloys with different chemical formulae, has been the subject of many research works [1–5]. These works have demonstrated that multiple irradiations of CrFeCoNiMo and $CoCrFeNiMo_{0.2}$ alloys by an electron beam with an energy density of 4 J/cm^2 and a pulse time of 1.5 μs induces the formation of a fusion zone. Moreover, its thickness expands with the increasing number of pulses [1,2]. The structure of this zone comprises crystals with an average size of 109 nm. Several authors [3–5] revealed that high-entropy alloys (HEAs) synthesized in selective electron-beam melting are characterized by high mechanical properties, which are possible due to the formation of micro-and nanodimensional structures and phases. One of the most probable mechanisms responsible for their forming is thought to be various hydrodynamic instabilities, e. g. the Mullins-Sekerka instability [6], thermocapillary instability [7,8] and the Kelvin-Helmholtz instability [9,10]. An assumption was made [11,12] that micro-and nanostructure phase states develop in multicomponent alloys owing to the evolving combination of thermal, concentration-evaporation and thermoelectric instabilities. This study investigates the effect of an electron beam with the energy density from 10 to 30 J/cm^2 and a pulse time of 200 μs on the AlCoCrFeNi high-entropy alloy (chemical composition, mass.%: 15.64 Al, 7.78 Co, 8.87 Cr, 22.31 Fe, 44.57 Ni). A principal method to analyze the structure of a material surface was selected scanning electron microscopy. Fig. 1 provides findings of an SEM-analysis carried out on the surface irradiated by an electron beam with an energy density of 30 J/cm^2. It is apparent from this figure that a cellular structure ranging

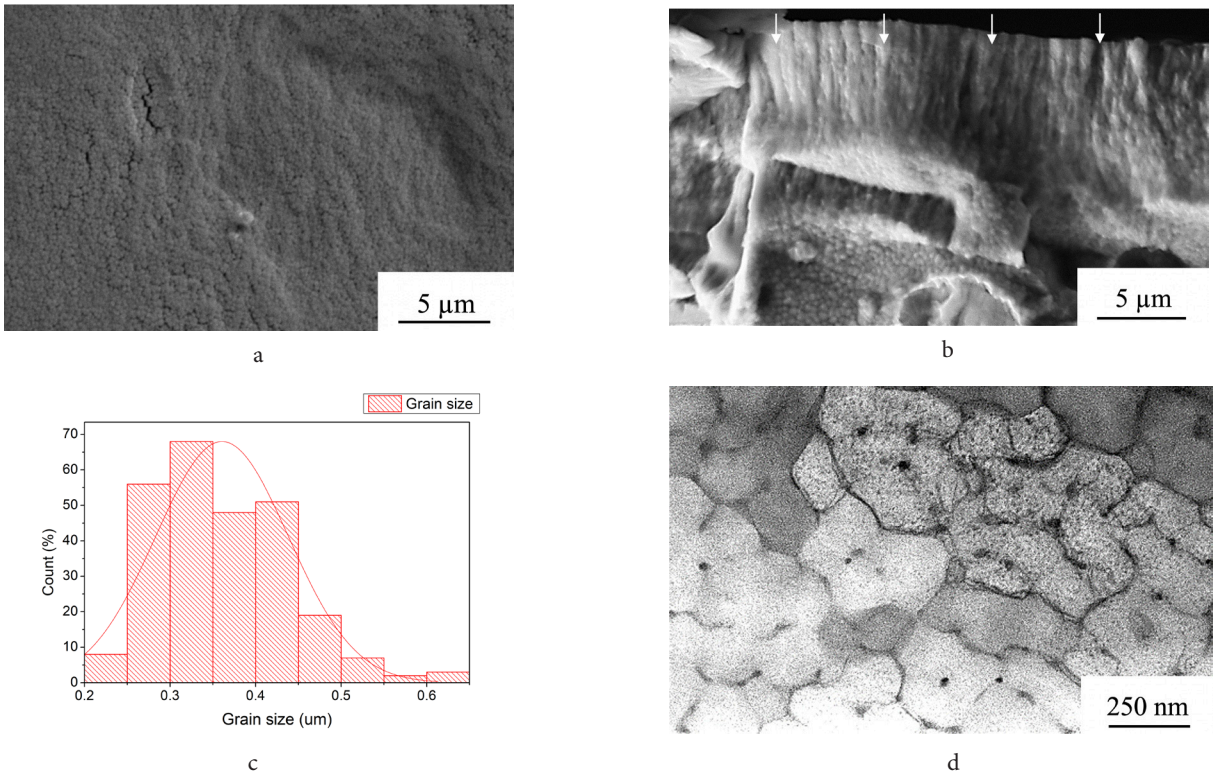

Fig. 1. Structure of a high-entropy alloy irradiated by an electron beam with an energy density of 30 J/cm^2 (SEM-image of the irradiated surface (a), SEM-image of the fracture surface (arrows show the direction of electron beam irradiation) (b), histogram of the grain size distribution of the irradiated surface (c), cross-section TEM-image of the irradiated surface(d)).

from 225.83 to 618.87 nm was formed on the treated surface. The dimensional distribution of cells displays one maximum in the range from 300 to 350 nm.

The cross-section of the samples (Fig. 1) was analyzed, and a conclusion was drawn that the modified layer is a product of the electron-beam treatment. The thickness of this layer depends on the height of the crystallization columns and increases with the growing energy density of an electron beam.

2. Results and Discussion

As discussed above, the formation of micro-and nano-dimensional structure and phase states on the surface during electron-beam treatment is induced by the combination of thermal-capillary, concentration-capillary and thermoelectric instabilities. We assume that this instability arises when an electron beam is applied to high-entropy alloys. The significant role of thermoelectric convection for the formation of a cellular crystallization structure is traced in the thickness of the molten layer ~1–20 μm. As stated in previous studies [13,14], thermoelectric effects fail to be neutralized totally by the thermocapillary convection if a concentrated flow of energy is supplied from above. When determining the thermoelectric coefficient, we proceed from the assumption that the convective flow, intensifying the thermoelectric effect, is of significant importance for the transfer of charge in the liquid state [12].

The dispersion equation, proposed earlier in [12], is used to determine conditions under which the combined instability is most likely to develop:

$$R_T - R_E - R_V - R_\sigma = 0, \tag{1}$$

$$R_\sigma = \omega^2\left(\left(\omega+2\omega_\nu\right)^2+\omega_c^2\right)-\frac{4\omega^2\omega_\nu^2 k_1}{k},$$

$$R_T = \omega_T\omega_\nu\left(\delta\left(1-\frac{k_1}{k_2}\right)\left(2\omega\omega_\nu+\omega^2+\omega_c^2\right)+\right.$$
$$\left.+\left(1-\frac{k}{k_2}\right)\left(\frac{2k_1\omega\omega_\nu}{k}+\omega_c^2\right)\right),$$

$$R_E = -\omega_E\omega_\nu\omega\left(\left(1-\frac{k_1}{k}\right)\omega_\nu+\omega\right),$$

$$R_V = \omega_p\omega_\nu\left(\left(\delta\left(1-\frac{k_1}{k_2}\right)+\left(1-\frac{k}{k_2}\right)\right)\omega_E\omega_\nu+\right.$$
$$\left.+2\delta\omega\omega_\nu\left(1-\frac{k_1}{k_2}\right)+\left(2\omega_\nu+\omega\right)\omega\left(1-\frac{k}{k_2}\right)\right),$$

where R_σ, R_T, R_E, R_V — capillary, thermocapillary, thermoelectric and vapour part of dispersion equation respectively, $\omega_T=\sigma_T G_0/\rho\nu$ — thermocapillary frequence, $\omega_\nu=\nu k^2$ — viscosity frequency, $\omega_c^2=\sigma_0 k^3-\varepsilon\varepsilon_0 E_0^2)/\rho$ — capillary frequence, $\omega_p=p'_\nu G_0/\rho\nu k$ — vapour-capillary frequency, $\omega_E=\varepsilon_0 E_0^2/\rho\nu$ — thermoelectric frequency, $k_1=\sqrt{k^2+(\omega/\nu)}$, $k_2=\sqrt{k^2+(\omega/\chi)}$, $\delta=\mathrm{Pr}/(1-\mathrm{Pr})$, $\mathrm{Pr}=\nu/\chi$ — Prandtl number, σ_0 — surface tension at a temperature of material melting T_m, σ_T — temperature coefficient of the surface tension, ρ — density, ν — kinematic viscosity, χ — temperature conductivity, G_0 — gradient of temperature, where ε — dielectric permittivity, ε_0 — electric constant, E_0 — electric field strength on the stable horizontal surface of a liquid. Provided that $\mathrm{Pr}\ll 1$ the Eq. (1) is written:

$$\frac{\omega_T\,\mathrm{Pr}}{2}(2\omega\omega_\nu+\omega_c^2)\left(\omega+2\omega_\nu\left(1-\frac{k_1}{k}\right)\right)+$$
$$+\frac{\omega_p\,\mathrm{Pr}}{2}\left(\omega_E\omega_\nu\left(\omega+2\omega_\nu\left(1-\frac{k_1}{k}\right)\right)+\right.$$
$$\left.+\omega\left(\omega^2+2\omega\omega_\nu+4\omega_\nu^2\left(1-\frac{k_1}{k}\right)\right)\right)-$$
$$-\omega_E\omega_\nu\omega\left(\left(1-\frac{k_1}{k}\right)\omega_\nu+\omega\right)-$$
$$-\omega^2\left(\left(\omega+2\omega_\nu\right)^2+\omega_c^2\right)+\frac{4\omega^2\omega_\nu^2 k_1}{k}=0. \tag{2}$$

Substituting $z=\frac{k_1}{k}$ and $\omega=\omega_\nu(z^2-1)$, the Eq. (2) is stated:

$$\left(C^2+2(z^2-1)\right)C_2+\left(2C_4+(z^2+2z+3)(z^2-1)\right)C_3-$$
$$-2(z^2+1)C_4-(z+1)^2\left(C^2+(z^2+1)^2-4z\right)=0, \tag{3}$$

where $C=\omega_c/\omega_\nu$, $C_2=\omega_T\mathrm{Pr}/2\omega_\nu$, $C_3=\omega_E/2\omega_\nu$, $C_4=\omega_E/2\omega_\nu$. As proposed earlier [12], such solutions are selected, which meet the condition $\mathrm{Re}(\omega)>0$ and $\mathrm{Re}(z)>0$. In these cases, the growth rate of perturbations $\alpha=\mathrm{Re}(\omega)>0$. The data for calculations is given in Table 1.

The values of specific heat of fusion and evaporation in the first approximation are determined according to the mixture rule: $X=\sum_{i=1}^{5}a_i x_i$, where a_i — volume percentage of an i-component in the alloy, x_i — specific heat of fusion (specific heat of evaporation) for an i-component of the alloy. The temperature gradient is found as in [12]: $G_0=((q-q_{out})/\kappa)$, where $q=E_s/t_0$ — energy density of an electron beam, E_s — surface energy density of an electron beam, q_{out} — evaporation-conditioned surface energy density, κ — thermal conductivity of a liquid metal. The role of evaporation for the power density [15] is calculated as follows: $q_{out}=10^6\left((A_{out}/\sqrt{2\pi k_B T_m m})\exp\left((A_{out}/k_B)(1/T_V-1/T_m)\right)\right)$, where A_{out} — work function of an atom escaping from the melt, k_B — Boltzmann constant, m — atomic mass, T_V — evaporation temperature.

The role of evaporation in the formation of nanostructures was calculated according to the previously proposed heat model [16], which considers this phase transformation. Fig. 2 provides the data on the temperature distribution over time at various depths from the irradiated surface at 30 J/cm².

It can be apparent from the data in this figure that the temperature on the irradiated surface is equal to the temperature of evaporation for this value of the energy density, whereas no evaporation is observed for any other values of the energy density below 30 J/cm². Therefore, for $E_s<30$ J/cm² we consider $\omega_p=0$.

Further, it is necessary to find the minimum wavelength, which initiates the combined instability. For this purpose, the solution (3) is determined in $z^2=-1\pm iC+\tilde{\omega}$. As a result,

Table 1. Thermal physical properties of AlCoCrFeNi systems [17–20].

Symbol / dimension	AlCoCrFeNi	Property
T_L, K	1768	Melting temperature
T_V, K	2100	Evaporation temperature
ρ_s, kg/m^3	7000	Solid phase density
ρ_L, kg/m^3	6890	Liquid phase density
ρ_V, kg/m^3	6700	Vapor phase density
ν, 10^{-7}m^2/s	6.56	Viscosity
χ, 10^{-5}m^2/s	1.5	Thermal diffusivity
σ, N/m	1.55	Surface tension
σ_T, 10^{-3}N/(m·K)	−0.1	Temperature coefficient of surface tension
κ_S, W/(m·K)	11	Thermal conductivity of solid phase
κ_L, W/(m·K)	281	Thermal conductivity of liquid phase
κ_V, W/(m·K)	290	Thermal conductivity of vapor phase
L_s, kJ/kg	309	Specific heat of melting
L_V, kJ/kg	6892	Specific heat of evaporation

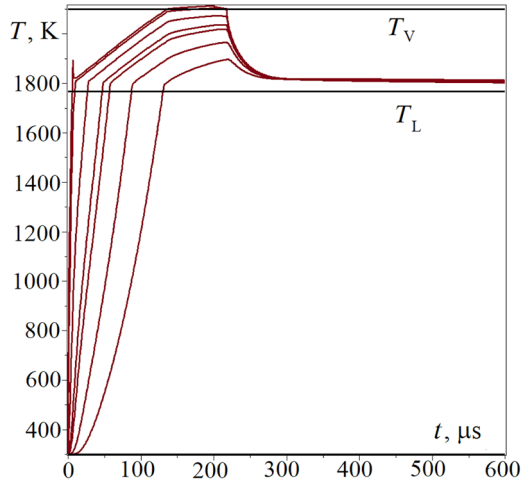

Fig. 2. Temperature distribution vs. time throughout the depth for the energy density $E_s = 30$ J/cm^2.

certain corrections for the frequency of capillary waves are obtained, which depend on thermal, evaporation-capillary and thermoelectric effects.

$$z^2 = -1 \pm iC - \frac{C_2}{2} + \frac{C_3}{2} + C_4. \quad (4)$$

Turning to (4) from z to ω, it is obtained:

$$\omega = -2\omega_\nu - \frac{\omega_T \,\mathrm{Pr}}{4} + \frac{\omega_p \,\mathrm{Pr}}{4} + \frac{\omega_E}{2} \pm i\omega_c. \quad (5)$$

Thermophysical constant variables and parameters of the electron beam were substituted, and it was concluded that the instability arises at $\lambda > 203$ μm for $E_s = 30$ J/cm^2 and without evaporation thermoelectric effects. The numerical solution of Eq. (3) shows that the thermocapillary instability arises at $\lambda > 210$ μm. Given the evaporation pressure equals 10^5 Pa, the instability begins with a wavelength of $\lambda = 43$ μm; numerical calculations confirm this. The instability for wavelengths ranging from 220 to 300 nm, which are equated to the sizes of crystallization cells under the experimental study, was initiated at an evaporation pressure of $4.5 \cdot 10^{11}$ Pa and $2 \cdot 10^{11}$ Pa.

The numerical solution of the dispersion Eq. (3) showed that the maximum value of the perturbation growth rate under these conditions falls on the wavelengths of 380 and 530 nm (Fig. 3 a, curve 1 and 2). Considering thermoelectric effects, the wavelength attributed to the origination of instability is 225 nm (Fig. 3 a, curve 3) for an evaporation pressure of 10^5 Pa and a thermoelectric coefficient of 4.3 V/K; this outcome is in line with experimental data.

The maximum growth rate is recorded for a wavelength of 430 nm; it differs slightly from the SEM data of the cellular structure. As mentioned above, the presented results are obtained in the low-frequency approximation by finding a solution to Eq. (3). We turn to the discussion of numerical solutions to full dispersion Eq. (1). This equation is a cumbersome algebraic equation of the 16th degree with respect to z_1, so we omit it here. The study considers only such roots of Eq. (1), which meet the condition $\mathrm{Re}(\omega) > 0$ and $\mathrm{Re}(z_1) > 0$, $\mathrm{Re}(z_2) > 0$. As numerical solution shows, the equation has two roots. In both cases, the instability arises at $\lambda > 220$ nm, and the maximum growth rate is registered for a wavelength of 430 nm (Fig. 3 b, curve 1); this is in line with the experimental data and solutions of Eq. (3).

This fact allows one to conclude that the low-frequency approximation is adequate (3). If evaporation is not taken into account, the wavelength at which the maximum growth rate is observed is the same as at an evaporative pressure of ~10^{11} Pa. This allows us to conclude that the thermoelectric instability prevails over the evaporative-capillary instability in this range of vapour recoil pressures. The most noticeable effect of evaporation becomes at an evaporative pressure of ~10^{10} Pa (Fig. 3 b, curve 2). The maximum growth rate, in this case, will be observed at a value of $\lambda_m = 450$ nm.

Fig. 4 demonstrates the correlation between the wavelength with the maximum growth rate and the energy density varying from 10 to 30 J/cm^2. This figure shows that the growing energy density E_s brings about a decrease in the wavelength according to the power-law $\lambda_m = 583.16 \cdot E_s^{-2.125}$ (correlation coefficient 0.999); therefore, the most likely expected sizes of the cellular crystallization structure will be reduced. This correlation allows optimizing the processing conditions of high-entropy alloys by low energy high current electron beams.

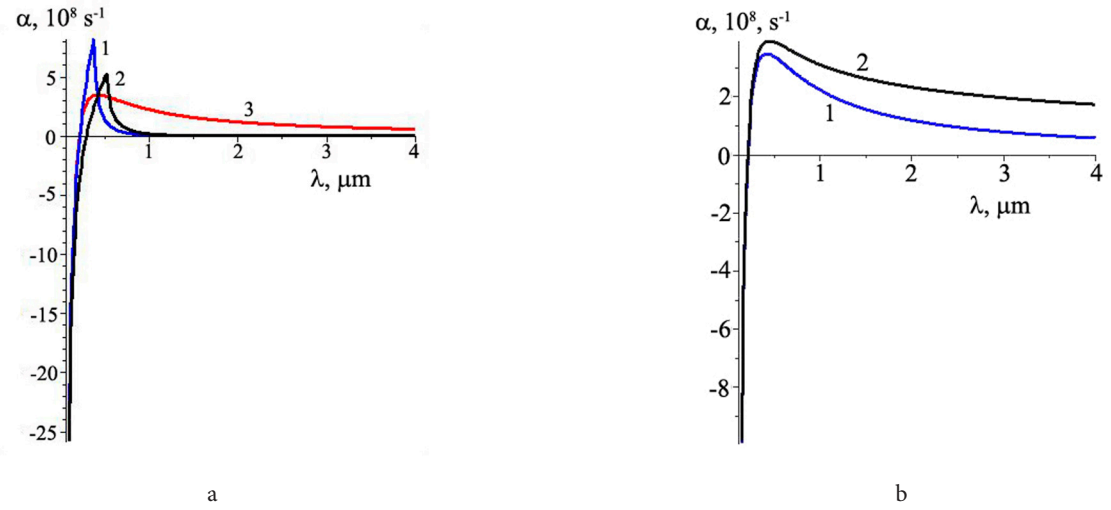

a b

Fig. 3. (Color online) The growth rate of perturbations on the melt surface vs wavelength under the application of an electron beam with an energy density of 30 J/cm^2 taking into account evaporation (curve 1 and 2) and evaporation and thermoelectric effects (curve 3) (a); The dependence of the growth rate of the melt surface perturbations on the wavelength, taking into account evaporation and thermoelectric effects, obtained by numerically solving the dispersion Eq. (1). Curve 1 corresponds to the value of evaporative pressure of 10^5 Pa, and curve 2 — 10^{10} Pa (b).

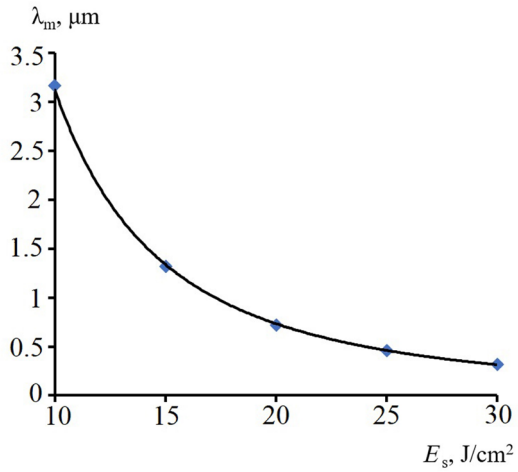

Fig. 4. Wavelength with the maximum growth rate vs energy density of the electron beam.

Still, it necessitates the research into the role of the concentration of alloying elements for the surface tension of the alloy under study and the determination of the diffusion coefficients in these alloys.

3. Conclusion

The study establishes that thermoelectric phenomena significantly affect the initial stage of thermocapillary flow instability in a high-entropy alloy melt irradiated by electron beams. The critical outcome of the study is that evaporation-capillary instability is possible only for the energy density of 30 J/cm^2 and higher. The correlations between the growth rate of perturbations at the plasma-melt boundary and the wavelengths display one maximum only, which is recorded in the submicro- and nanometer range for the thermoelectric coefficient $\gamma \geq 4$ V/K. Due to the obtained results, the mechanism responsible for forming surface micro-and nanostructures represents the combination of thermal, evaporation-capillary and thermoelectric instabilities. They can be relevant for determining the optimal conditions of electron-beam processing high-entropy alloys to form micro-and nanostructures. The further development of the model can be related to the consideration of concentration-capillary effects.

Acknowledgements. The work is performed under the financial support of the Russian Science Foundation [No. 20-19-00452].

References

1. P. Lyu, Y. Chen, Z. Liu, J. Cai, C. Zhang, Y. Jin, Q. Guan, N. Zhao. Appl. Surf. Sci. 504, 144453 (2020). Crossref
2. P. Lyu, T. Peng, Y. Miao, Z. Liu, Q. Gao, C. Zhang, Y. Jin, Q. Guan, J. Cai. Surf. & Coat. Tech. 410, 126911 (2021). Crossref
3. V. V. Popov, A. Katz-Demyanetz, A. Koptyug. Heliyon. 5 (2), e01188 (2019). Crossref
4. K. Kuwabara, H. Shiratori, T. Fujieda, K. Yamanaka, Y. Koizumi, A. Chiba. Add. Manufactur. 23, 264 (2018). Crossref
5. A. Munitz, S. Salhov, S. Hayun, N. Frage. J. of Alloys and Compounds. 683, 221 (2016). Crossref
6. S. Li, J. S. Lowengrub, P. H. Leo, V. Cristini. J. Crys. Growth. 277, 578 (2005). Crossref
7. H. Liu, Z. Zeng, L. Yin, Z. Qiu, L. Qiao. Inter. Comm. in Heat and Mass Transf. 121, 105099 (2021). Crossref
8. L. A. Dávalos-Orozco. Inter. J. of Non-Linear Mech. 109, 15 (2019). Crossref
9. L. A. Bulavin, V. I. Tkachenko. Ukr. J. Phys. 63, 747 (2018). Crossref
10. W. Sun, J. Y. Zhong, S. Zhang, B. W. Tong et al. High Energ. Density Phys. 31, 47 (2019). Crossref
11. V. Sarychev, S. Nevskii, S. Konovalov, A. Granovskii, V. Gromov. Mater. Res. Expr. 6 (7), 076551 (2019). Crossref

12. S. Nevskii, V. Sarychev, S. Konovalov, A. Granovskii, V. Gromov. Metals. 10, 1399 (2020). Crossref
13. E. D. Eidelman. Phys.-Uspekhi. 38, 1231 (1995). Crossref
14. E. D. Eidelman. Tech. Phys. 43, 1275 (2008). Crossref
15. R. V. Arutyunyan, V. Yu. Baranov, L. A. Bol'shov et al. Effects of laser radiation on materials. Moscow, Nauka (1989) 367 p. (in Russian) [Р. В. Арутюнян, В. Ю. Баранов, Л. В. Большов и др. Воздействие лазерного излучения на материалы. Москва, Наука (1989) 367 с.]
16. V. Sarychev, S. Nevskii, S. Konovalov, A. Granovskii, Y. Ivanov, V. Gromov. Mater. Res. Expr. 6 (2), 026540 (2019). Crossref
17. S. Uporov, V. Bykov, S. Pryanichnikov, A. Shubin, N. Uporova. Intermetallics. 83, 777 (2019). Crossref
18. S. Rohila, R. B. Mane, G. Ummethala, B. B. Panigrahi. J. Mater. Res. 34, 1 (2017). Crossref
19. Critical Melting Points and Reference Data for Vacuum Heat Treating (Ed. by V. Osterman, H. Antes Jr.) Fontana, Solar Atmosphere (2010) 42 p.
20. V. I. Nizhenko, L. I. Floka. Surface tension of liquid metals. Moscow, Metallurgiya (1981) 208 p. (in Russian) [В. И. Ниженко, Л. С. Флока. Поверхностное натяжение жидких металлов и сплавов. Москва, Металлургия (1981) 208 с.]